



**CHALMERS**  
UNIVERSITY OF TECHNOLOGY

## Dual-Polarised Radiometer for Road Surface Characterisation

Downloaded from: <https://research.chalmers.se>, 2024-04-19 16:44 UTC

Citation for the original published paper (version of record):

Auriacombe, O., Vassilev, V., Pinel, N. (2022). Dual-Polarised Radiometer for Road Surface Characterisation. *Journal of Infrared, Millimeter, and Terahertz Waves*, 43(1-2): 108-124.  
<http://dx.doi.org/10.1007/s10762-022-00847-5>

N.B. When citing this work, cite the original published paper.



# Dual-Polarised Radiometer for Road Surface Characterisation

Olivier Auriacombe<sup>1</sup> · Vessen Vassilev<sup>1</sup> · Nicolas Pinel<sup>2</sup>

Received: 17 September 2021 / Accepted: 8 March 2022 / Published online: 21 March 2022  
© The Author(s) 2022

## Abstract

This paper presents measurements using a dual-polarised radiometer operating at 93 GHz to detect ice or water on asphalt in laboratory conditions. The brightness temperatures of both  $H$  and  $V$  polarizations were measured for a dry surface, liquid water, and ice on asphalt at observation angles of  $50^\circ$  and  $56^\circ$ . The results presented in this paper demonstrate that the studied road conditions can be identified by the radiometer. The measurements are compared with a model and surface parameters, such as dielectric constant and roughness are fitted and compared to reference values. The experiments and results, described in this article, are the first steps towards the future installation of a polarimetric sensor on a moving vehicle for traffic safety.

**Keywords** Microwave · Terahertz · Radiometer · Schottky diodes · Polarization · Remote sensing · Sky · Brightness temperature · Ice · Water · Asphalt · Road · Polarimetry · Reflection · Emission

## 1 Introduction

Knowledge of road surface conditions is important for road traffic safety and essential for future autonomous drive applications. Technologies to detect wet, icy, or snowy asphalt roads are of major interest for the automotive industry and governments to reduce the number of fatalities and damages linked to weather accidents. In the USA, 1,836 deaths, 136,309 injuries, and 536,731 car accidents were reported on average per year due to snowy and icy roads [1, 2]. A thin transparent ice layer, the so-called black ice, is the main cause of such accidents as it is hardly visible by human eyes. The black ice generally forms when moisture from rain or fog freezes on road surfaces.

---

✉ Olivier Auriacombe  
oliaur@chalmers.se

<sup>1</sup> Chalmers University of Technology, Göteborg, Sweden

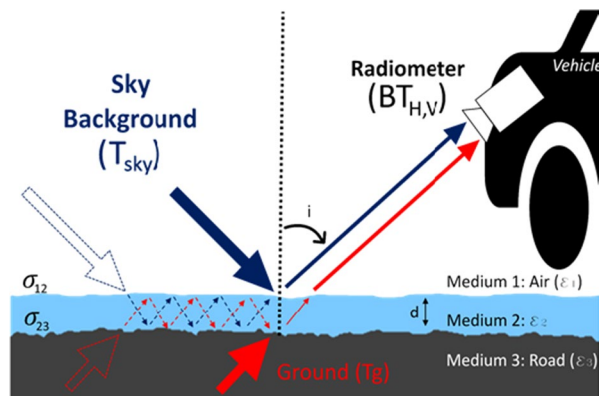
<sup>2</sup> Icam Ouest School of Engineering—Nantes Campus, Carquefou, France

The recognition of road conditions is done by either installing hardware within roads, on moving vehicles, or on structures above bridges and motorway sections. In-pavement methods use multiple sensors built in the road to measure the presence of ice [3–5]. Black ice can appear in certain spots and may not cover the entire surface of the road; therefore, a high number of embedded sensors are required to cover different sections of the road. This results in high installation and maintenance costs. Another technique is to use “weather stations” [6] around dangerous areas. Although this technique gives a good warning on the potential presence of ice, it does not reflect real conditions above the roads, resulting in false alarms. Infrared methods [7–9] and detectors based on camera image recognition [10, 11] can determine efficiently the road conditions but are highly dependent on weather conditions (mist, fog, rain) and illumination (daylight or night). Bistatic radars [12, 13] or monostatic radars [14, 15] can also be used to monitor road conditions. They are based on the measurements of backscattering coefficients for vertical, horizontal, and cross polarizations for each road surface. Stokes parameters [16] or target entropy [17] can be determined permitting the differentiation of the surfaces. However, a polarimetric radar measurement requires a statistical approach to gather a reliable estimate of the surface properties, requiring measuring the same area many times.

Passive radiometers are commonly used in remote sensing to monitor landscapes such as soil moisture [18], sea surfaces [19, 20], or retrieve data for weather predictions [21, 22]. Polarimetric radiometers could also be installed on moving vehicles or motorway structures for road condition monitoring. The detection principle is to measure the radiometric brightness temperatures at two orthogonal polarizations ( $BT_{H,V}$ ), as shown in the schematic in Fig. 1. A surface property is accounted either by its “reflectivity” ( $R_{H,V}$ ) or “emissivity” ( $E_{H,V}$ ) which are related to each other as  $R_{H,V} + E_{H,V} = 1$ . The reflectivity of each road condition depends on the polarization ( $H$  and  $V$ ), the dielectric constants ( $\epsilon$ ), the thickness of the layer ( $d$ ), the angle of observation ( $i$ ), and the roughness of the surfaces ( $\sigma_{12}$  and  $\sigma_{23}$ ).

The measured brightness temperature by the radiometer is a combination of reflected sky and emitted ground radiations as shown in Eq. (1). By measuring the brightness temperature of the surface and knowing its physical temperature ( $T_{\text{ground}}$ ) and the

**Fig. 1** Schematic of a polarimetric radar observation. The sky/ground radiations ( $T_{\text{sky}}$  and  $T_{\text{ground}}$ ) reflect and get transmitted at each interface between the layers. The radiometer measures the combination of reflected sky and transmitted ground temperatures for each polarization. The dielectric properties of media 2 and 3 ( $\epsilon$ ), the angle of observation ( $i$ ), and the surface roughness ( $\sigma$ ) impact the reflection/transmission coefficients



temperature of the unpolarised sky radiation ( $T_{\text{sky}}$ ), the reflectivity ( $R_{H,V}$ ) and emissivity ( $1-R_{H,V}$ ) of the surface can be calculated. Equation (1) is valid for planar surfaces in coherent scattering model. This formula can be extended to layers with small surface roughness by replacing the planar reflectivity ( $R_{H,V}$ ) with a reflectivity which includes the roughness term ( $R_{H,V\text{rough}}$ ). This mechanism is described in detail in Sect. 4. Since ice and water have different dielectric constants, the expected surface reflectivity/emissivity are expected to change when the surface is covered by water or ice.

$$BT_{H,V} = (1 - R_{H,V}) \times T_{\text{ground}} + R_{H,V} \times T_{\text{sky}} \quad (1)$$

Within some frequency windows ( $40 \pm 10$  GHz,  $90 \pm 20$  GHz,  $150 \pm 20$  GHz, etc.), water vapour does not have spectral absorption lines keeping the sky brightness temperature ( $T_{\text{sky}}$ ) much colder than the terrestrial temperature. Higher frequency allows for more compact and directive antennas resulting in smaller sensing spot. Frequencies between 70 and 100 GHz are attractive for surface characterization as one can build sensitive radiometers while the sky temperature remains low and relatively independent of weather conditions. For example, statistical measurements at 85 GHz for the west coast of Sweden show that the sky temperature is below 100 K over 85% of the time [23]. As the sky and ground brightness temperatures have a radiometric difference of more than 140 K, the polarimetric characterization of the surface properties results in a good “contrast” between road conditions relaxing the requirements on temperature resolution of the radiometer. Another benefit of radiometers at these frequencies is that they can give instantaneous measurements of the road properties without being affected by weather conditions or external illuminations. The first instrument based on this technique was developed in 1999 by Macelloni et al. [24] and consisted of two dual-polarised radiometers operating at 10 and 37 GHz. Later, Sasada et al. [25] presented a dual-polarised radiometer at 95 GHz with a system noise temperature of 2000 K and acquisition time of 500 ms, placed above a road. However, those instruments were not sensitive enough to properly distinguish all road conditions effectively.

In this paper through laboratory measurements, we study the feasibility of using a 93 GHz dual-polarised radiometer as a sensor for road surface recognition. This paper is organised as follows. Section 2 describes the radiometer and the laboratory experiments on dry asphalt, liquid water-covered, and ice-covered asphalt. Section 3 presents the radiometric results in  $H$  and  $V$  polarizations for the three road conditions (dry, liquid water, ice). In Sect. 4, a scattering model is used to study the effect of the surface parameters by fitting the results obtained in Sect. 3. The model and results are also shown in terms of their emissivity for each road condition in Sect. 4 before concluding in Sect. 5.

## 2 Laboratory Experiments

### 2.1 Radiometer

The instrument is a double sideband dual-polarised radiometer composed of two heterodyne receivers, a local oscillator, and a power meter at the backend. The

schematics of the radiometer are shown in Fig. 2. A dual-polarised horn circular antenna is followed by an orthomode transducer, which separates the  $H$  and  $V$  polarizations and feeds them to their corresponding receiver. Both receivers are composed of low noise amplifiers (LNA), with 22 dB gain from 72 to 105 GHz. Subharmonic mixers (SHM) are then used combined with a local oscillator source (LO) to down-convert the RF signal between 87.2 and 98.4 GHz to a lower intermediate frequency (IF) from 1.0 to 5.6 GHz. The LO chain comprises a voltage control oscillator with phase-locked loop at 11.6 GHz, two active commercial multiplier modules (HMC-032 and HMC-034), and a splitter to deliver similar LO signals at the input of the  $H$  and  $V$  SHMs. The IF is amplified by a 38 dB gain LNA, followed by a band-pass filter. A power meter (U2002A, Keysight) combined with an RF switch measures the powers from the  $H$  and  $V$  branches every 7 ms.

A lens, positioned at the horn aperture, is focusing the beam at a focal length of 520 mm. A linear motor is used to place an absorber in front of the feedhorn at the beginning of the measurement to measure the system noise temperature for calibration purposes. A proportional integral derivative (PID) controller, with thermally insulated heaters and temperature sensors, was used to set and maintain the radiometer's operating temperature constant. Because of the radiometer's thermal stability (0.5 K variation over one hour of measurement), no periodical calibration is needed to obtain the absolute measurement of the brightness temperature throughout the duration of the experiment [26].

The system noise temperate of the radiometer was measured using the Y-factor method looking at an absorber immersed in liquid nitrogen (77.3 K) and a room temperature absorber (around 295 K). Typically, the noise temperature is  $518.1 \pm 4.3$  K and  $498.6 \pm 4.1$  K for the H-pol and V-pol, respectively.

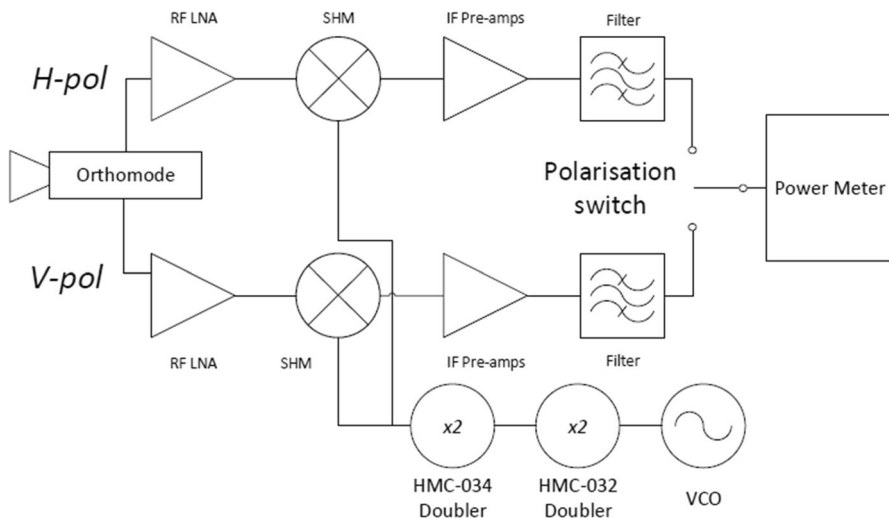


**Fig. 2** Functional diagram of the dual-polarised radiometer

## 2.2 Asphalt Surface

The studied surface is composed of stone mastic asphalt with an aggregate size of about 8 mm. The surface area was measured using a Handyscan 3D laser scanner with 0.025 mm accuracy. Figure 3 shows a picture of the surface used for the measurements (left) and its 3D scan model (right). The parameters of the surface were measured on a  $50 \times 50$  mm area corresponding to the beam spot size observed by the radiometer on the surface.

The height probability density function and correlation function were retrieved from the 2-dimensional height profile [27]. The main parameters from those functions are the rms height ( $s$ ) and the correlation length ( $l_c$ ), respectively. They correspond to the height standard deviation and the distance between two locations considered statistically uncorrelated, respectively. A Gaussian function was used to fit the density function (coefficient of determination ( $R^2$ ) of 97.32%) and the correlation function ( $R^2$  of 99.27%). The Gaussian shape is mainly used for modelling of electromagnetic scattering from random rough surfaces [28]. The Gaussian fit applied to the correlation function is shown in Fig. 4. The studied asphalt surface has a rms height of  $s = 0.65 \pm 0.03$  mm and a correlation length of  $l_c = 2.54 \pm 0.03$  mm.

## 2.3 Experimental Setup

The experimental setup is shown in Fig. 5. The asphalt surface is placed at 50 cm from the instrument, corresponding to the focal length of the dual-polarised radiometer (described in Sect. 2.1). In this study, two observation angles were selected,  $50^\circ$  and  $56^\circ$ . A liquid nitrogen Dewar filled with microwave absorber (ECOSORB) is used to represent the sky background brightness temperature ( $T_{\text{bkg}}$  in Fig. 1). The background brightness temperature is measured by placing a flat aluminium reflector on the asphalt surface (Fig. 5). The  $H$  and  $V$  background brightness temperatures were measured identical,  $T_{\text{bkg}} = 97.7 \pm 0.5$  K, for  $H$  and  $V$  at both  $50^\circ$  and  $56^\circ$ . Once the background temperature was acquired, the aluminium reflector, shown in Fig. 5,



**Fig. 3** Asphalt road surface used in the study (left) and its 3D scan (right)

**Fig. 4** Autocorrelation function of the asphalt surface where  $\xi$  is the displacement between two points on the surface

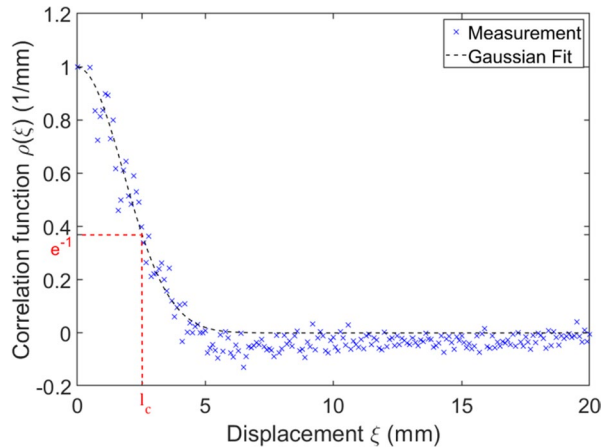
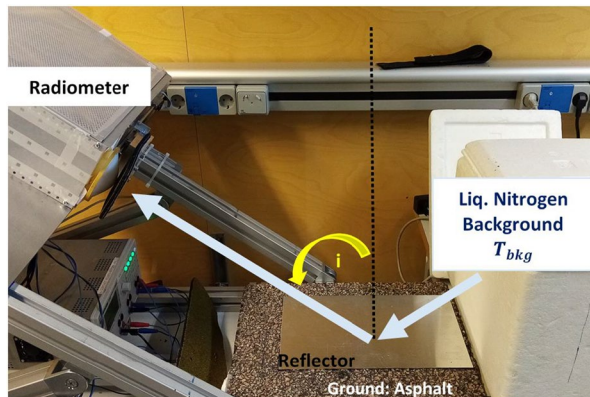


**Fig. 5** The experimental setup. The radiometer is measuring the background brightness temperature with a reflector placed on top of the road surface



was removed to measure the  $H$  and  $V$  brightness temperatures of various asphalt conditions (dry, wet, ice).

## 2.4 Surface Preparation

The brightness temperatures are measured for dry, water covered, and icy surfaces and are shown in Fig. 6. In the case of the dry asphalt measurements, the range of asphalt physical temperatures is varied from around 250 to 290 K. The coldest temperature is reached by spraying the surface with liquid nitrogen. For the study of the liquid water, 20 cl of water is poured on the dry asphalt. The water is then slowly drained to reduce its thickness to eventually only be a “wet” surface. Finally, the formation of the ice layers is performed in two steps. Firstly, the dry surface is cooled down to a low temperature (below 273 K) using liquid nitrogen. Then, liquid water (20 cl) is poured onto the cold dry surface. The water slowly freezes by thermal conduction, similarly to the formation of black ice. Once the ice is formed, the



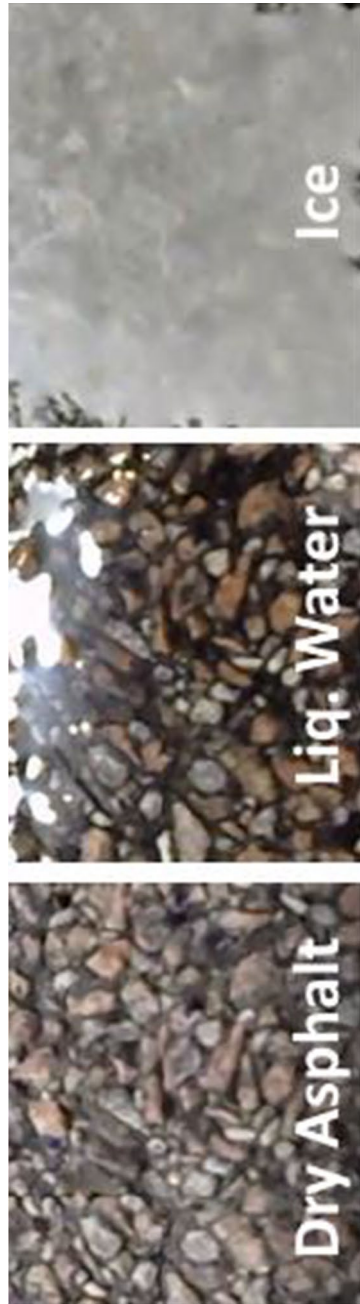


**Fig. 6** Surface conditions studied in a laboratory-controlled environment. From left to right are dry, water, ice on the asphalt surface



temperature of the ice is further decreased by spraying additional liquid nitrogen. The convection of the air in the laboratory slowly warms up the ice layer until it sublimates. Different thicknesses of ice are obtained by pouring a larger quantity of liquid water on the dry cold asphalt surface. Once the asphalt became dry, the entire process is repeated for studying different ice thicknesses.

### 3 Measurements Results

#### 3.1 Dry Asphalt

Measured brightness temperatures for  $H$  and  $V$  polarizations are shown in Fig. 7a, as the physical temperature of the surface is varied with time. At 50 s after the start of the measurement, liquid nitrogen is sprayed onto the surface, resulting in a drop of both H-pol and V-pol BTs. Eighty seconds after the start, the surface starts to warm up, and at 485 s, the warming is accelerated by heating the surface with hot air. The use of the heat gun is observable on the H-pol and V-pol BTs as an abrupt increase in their absolute values.

The same dataset is used in Fig. 7b, which shows the measured  $H$  brightness temperature as a function of the measured  $V$  brightness temperature. The minimum in H-pol BT corresponds to the lowest asphalt physical temperature (below 250 K) while the highest H-pol BT (in red) is measured when the asphalt temperature is 292 K. The linear slope measured can be verified by expressing the H-pol BT as a function of the V-pol BT, and  $T_{\text{sky}}$  and the  $H$  and  $V$  reflectivity's ( $R_{H,V}$ ) from Eq. (1),

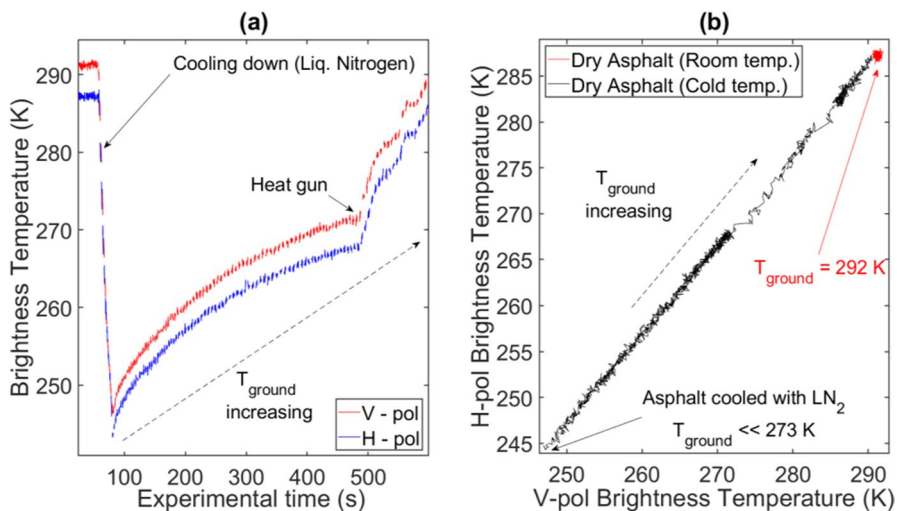


**Fig. 7** **a** Measurement sequence for the dry asphalt at 50° observation angle,  $V$  and  $H$  polarizations in red and blue, respectively. The surface is cooled down by spraying liquid nitrogen. **b**  $H$  brightness temperature as a function of the  $V$  brightness temperature measured from the left plot. The blue and red points are the calibration target and dry room temperature asphalt, respectively. The black curve corresponds to the cold asphalt warming up

shown in Eq. (2). In the dry asphalt experiment, only the temperature of the asphalt is changing resulting in constant  $T_{\text{sky}}$  and  $H$  and  $V$  reflectivity's values. Therefore, the linear slope of H-pol BT as a function of V-pol BT is verified.

$$BT_H = \frac{(1 - R_H)}{(1 - R_V)} \times BT_V + \frac{R_H - R_V}{1 - R_V} \times T_{\text{sky}} \quad (2)$$

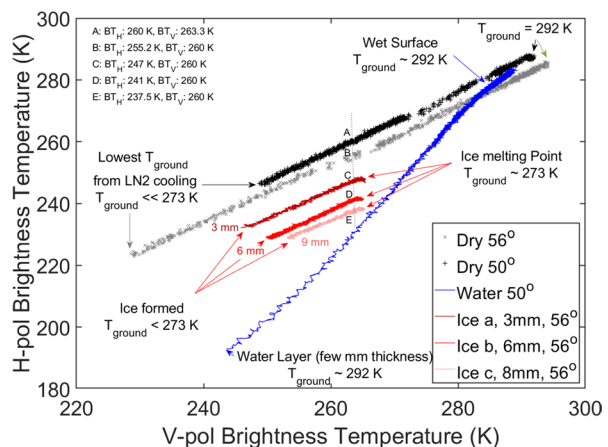
### 3.2 Dry Asphalt, Liquid Water, and Ice

The three road conditions described in Sect. 2.4 are measured independently with different observation angles and thicknesses. Summary of the results is shown in Fig. 8.

Dry asphalt measurements are performed with incident angles of  $56^\circ$  (grey curve) and  $50^\circ$  (black curve). The  $56^\circ$  experiment started with a lower asphalt physical temperature than the  $50^\circ$  measurement as more liquid nitrogen was sprayed onto the surface. The H-pol BT from the grey curve ( $56^\circ$ ) is offset by 3 to 5.5 K compared the black curve ( $50^\circ$ ). As expected, this comes from the fact that a small observation angle produces less difference between the  $H$  and  $V$  reflection coefficients, while other parameters remain identical.

The result for liquid water, with  $i=50^\circ$ , is shown in blue in Fig. 8. The thickness of the water layer varies from a few millimetres to only a wet surface, while the ground temperature is kept constant at 292 K. For a thick layer of water above the asphalt surface, the H-pol and V-pol BTs are 193 K and 244 K, respectively. It is the lowest H-pol and V-pol BTs measured. Indeed, a thick liquid layer acts as a low roughness reflector resulting in a low H-pol and V-pol BT values. As the water is drained, the H-pol and V-pol BT is increasing and, as the water dries out, the H-pol and V-pol BT is approaching the measurement for dry surface at the same observation angle (black curve). Moreover, the change of the water layer thickness

**Fig. 8** Measured H-pol–V-pol brightness temperatures for dry asphalt, liquid water, and ice with observation angles of  $50^\circ$  and  $56^\circ$



could be interpreted as a change of surface roughness of the air–water boundary, the thinner the layer, the higher the roughness. When the thickness of the water layer covering the surface is undistinguishable, only a wet asphalt surface remains. This causes a small variation in the slope between V-pol BTs of 278 K and 282 K. The effective dielectric constant of the wet surface is a mixture between the water and dry components. At 92.8 GHz and 19 °C, the water dielectric constant is  $\epsilon_{\text{water}} = 8.00 - 13.29 \times i$  [27] while a sample of Rock with binder at 11 GHz has a dielectric constant of  $\epsilon_{\text{asphalt}} = 6.0 - 0.14 \times i$  [30]. Depending on the mixing rules for asphalt, the effective dielectric constant changes as a function of the amount of mixed water molecules [28]. The disappearance of the thin film of water above the surface combined with the presence of water molecules embedded within the asphalt slightly change the H-V ratio from the surface. When the water component of the wet surface dries, the effective dielectric constant converges to the dry surface dielectric constant, corresponding to the intersection point between the blue curve and black curve at the highest V-pol BT (291 K) and H-pol BT of 289 K, in Fig. 8.

Finally, results from measurements of ice are shown in Fig. 8 in red, for an observation angle of 56°, with ice thicknesses of around 3 mm (ice a, dark red), 6 mm (ice b, pure red), and 8 mm (ice c, pink). The physical temperature of the ice is increasing from its formation (low H-pol, V-pol BTs) to its melting point at 273.15 K reached for the three sets of ice at V-pol BT of 266 K. No fluctuation within the linear trend (like for liquid water) is observed because the dielectric constant of the ice does not vary sensitively over temperature and the roughness's of the ices are remaining identical through the experiments. At 92.8 GHz, it is  $\epsilon_{\text{ice}} = 3.19 - i \times 8.5 \times 10^{-2}$ , at 0 °C and  $\epsilon_{\text{ice}} = 3.17 - i \times 5.8 \times 10^{-2}$  at -20 °C [27]. As the thickness of the ice increases, H-pol BT decreases for the same V-pol BT (points C, D, and E in Fig. 8). The thinnest 3 mm ice has the highest H-pol BT and least difference of 13 K between V and H BT compared to the thickest 8 mm ice where the difference is 22.5 K. This observation can be related to the roughness of the surfaces: the thinner ice will present rougher ice-air boundary, while thicker ice has a smoother, more specular surface producing higher degree of polarization. These values can be compared to the dry asphalt (point B) where the difference is only 4.8 K.

#### 4 Radiometric Modelling

Models exist to calculate the electromagnetic scattering occurring at the interface between dielectric media. Modelling the expected brightness temperature for various conditions of the road (dry, wet, ice) is necessary to verify the measurements presented in this paper and can be used to evaluate the feasibility of identifying other surfaces with different surface parameters.

The reflectivity ( $R_{\text{HorV}}$ ) in Eqs. (1) and (2) is calculated as a function of the dielectric constants of the media (asphalt, liquid water, or ice), the surface roughness between two dielectric media, the thickness of the dielectric layer, the observation angle, and the frequency range of the radiometer. The difficulty of simulating a road surface comes from the fact that a surface on each side of a layer is not perfectly flat but with a certain roughness ( $\sigma_{12}, \sigma_{23}$  see Fig. 1). The model

considered in this article is a general approach described in detail by Jonard et al. [29] and Tabatabaenejad et al. [30].

#### 4.1 Rayleigh Roughness of Uncorrelated Surfaces

Three assumptions were considered for modelling the scattering of a rough surface. Firstly, it is considered that at each point forming the boundary between the two dielectric media, the incident wave is reflected as if the boundary is a locally planar surface, with orientation given by the surface slope at considered point. This is known as the Kirchhoff-tangent plane approximation [31]. Secondly, the Rayleigh roughness criterion ( $\sigma_R$ ) defines the maximal electromagnetic roughness of a surface when only the coherent scattering contribution can be considered. The Rayleigh roughness criterion ( $\sigma_R$ ) is quantified by  $\sigma_R < \frac{\lambda}{8 \times \cos i}$ , where  $i$  is the observation angle and  $\lambda$ , the wavelength [32]. For observation angles of 50 and 56° at 92.8 GHz,  $\sigma_{R,\max}$  is 0.62 mm and 0.72 mm, respectively. In Sect. 2.2, the asphalt roughness was measured with a rms height of  $0.65 \pm 0.03$  mm. The measured surface roughness is lower or equivalent to the Rayleigh criterion, which permitted to consider only the coherent component of the reflectivity for the model. Finally, all surface height variations (roughness) are assumed to be uncorrelated.

In the absence of roughness, the reflection and transmission coefficients ( $r_{H,V}$ ,  $t_{H,V}$ ) are defined as per Eq. (3), with  $n_{u,v}$  the refractive indexes of the media  $u$  and  $v$ ,  $\theta_i$  and  $\theta_t$  the observation and transmission angles, respectively.

$$\begin{cases} r_{Huv,flat} = \frac{n_v \cos \theta_i - n_u \cos \theta_t}{n_v \cos \theta_i + n_u \cos \theta_t} \\ r_{Vuv,flat} = \frac{n_v \cos \theta_i - n_u \cos \theta_t}{n_v \cos \theta_i + n_u \cos \theta_t} \\ t_{H,Vuv,flat} = 1 + r_{Huv,flat} \\ t_{H,Vvu,flat} = 1 - r_{Hvu,flat} \end{cases} \quad (3)$$

The equivalent reflection coefficient ( $r_{H,V,rough}$ ) results from the sum of all the upward-moving waves in medium 2 between the rough surfaces ( $\sigma_{12}, \sigma_{23}$  in Fig. 1). It is a combination of the boundary reflection coefficients for flat surfaces, the roughness of those surfaces, observation angles, the vertical component of the propagation wavenumber ( $\Gamma_i = k_0 n_u \cos \theta_i$ ), and thickness of the middle layer ( $d$ ), expressed in Eq. (4) [32].

$$r_{H,V,rough} = r'_{H,V12} + \frac{t'_{H,V12} \times t'_{H,V21} \times r'_{H,V23} \times e^{-j2\Gamma_2 d}}{1 - r'_{H,V12} \times r'_{H,V23} \times e^{-j2\Gamma_2 d}} \quad (4)$$

The reflection and transmission coefficients for the rough surface  $r'$  and  $t'$  in Eq. (4) are detailed in Eq. (5) and depend on those for a flat surface and the surface roughness's.

$$\begin{cases} r'_{H,V12} = r_{H,V12,\text{flat}} \times \exp(-2\Gamma_1^2 \sigma_{12}^2) \\ r'_{H,V23} = r_{H,V23,\text{flat}} \times \exp(-2\Gamma_2^2 \sigma_{23}^2) \\ t'_{H,V12} = t_{H,V12,\text{flat}} \times \exp\left(-\frac{1}{2}(\Gamma_1 - \Gamma_2)^2 \sigma_{12}^2\right) \\ t'_{H,V21} = t_{H,V21,\text{flat}} \times \exp\left(-\frac{1}{2}(\Gamma_1 - \Gamma_2)^2 \sigma_{12}^2\right) \end{cases} \quad (5)$$

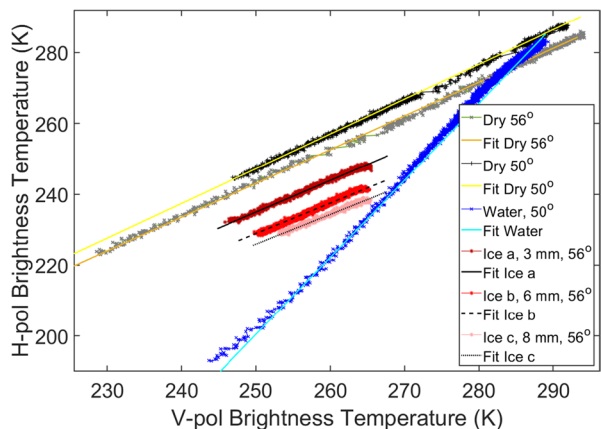
Once the equivalent reflection coefficients are calculated using Eq. (5), the corresponding reflectivity is retrieved ( $R_{H,V\text{rough}} = |r_{H,V\text{rough}}|^2$ ) and the brightness temperatures for the  $H$  and  $V$  polarizations are then calculated using Eq. (1).

## 4.2 Brightness Temperature Modelling

The model of the reflection coefficient, given by Eq. (4), is used to fit the measurements presented in Sect. 3.2. Firstly, the dry asphalt at  $50^\circ$  and  $56^\circ$  (dry a and b in Fig. 8) are fitted using various parameters such as the ground roughness, dielectric constant of the asphalt and ground temperature at fixed observation angles. Each H-pol and V-pol BTs is calculated with surface temperatures between 200 and 295 K. A matrix of reflection coefficients is created to find the best fit for the two angles. The asphalt surface roughness is varied between 0.4 and 1.0 mm with 0.001 mm steps and the asphalt dielectric constant from  $5.0 - 0.04 \times i$  to  $12.0 - 2.0 \times i$ , with 0.02 and 0.04 steps for the real and imaginary parts, respectively. For reference, a sample of Rock with binder at 11 GHz has a dielectric constant of  $\epsilon_{\text{asphalt}} = 6.0 - 0.14 \times i$  [34]. The best fits, using the least square method (shown in yellow in Fig. 9), are for an asphalt dielectric constant of  $\epsilon_{\text{asphalt}} = 8.9 - 0.72 \times i$  and an asphalt roughness of  $\sigma_{\text{asphalt}} = 0.668$  mm. This asphalt roughness corresponds to the measured roughness  $0.65 \pm 0.03$  mm (Sect. 2.2). The values obtained for  $\epsilon_{\text{asphalt}}$  and  $\sigma_{\text{asphalt}}$  are then used to model and fit the results from liquid water and ice.

Figure 9 shows the measured and modelled H-pol and V-pol BTs from dry, liq., water, and ices. All fitting parameters are summarized in Table 1. The main factor is the top surface roughness corresponding to the boundary air–liquid water or ice.

**Fig. 9** Measured  $H$ – $V$  brightness temperatures fitted with modelled brightness temperatures from dry asphalt, liquid water, and ice



The liquid water fit is obtained by selecting a ground and water temperature equal at 19 °C, as it is during the experiment. The parameter changing during the measurement is the thickness of the water layer which can be interpreted as an increase of the air–water boundary roughness, from 0 (few mm of water) to  $\sigma_{\text{asphalt}}$  (wet surface). The modelled BTs are matching the measured BTs, with similar starting and ending H-pol and V-pol BTs. A thick layer of liquid water has a low surface roughness while a thinner thickness is more affected by the ground roughness. Small fluctuations within the data (blue points in Fig. 9) around the modelled curve could arise from the fact that the water poured at the beginning of the measurement was lower than 19 °C and is warming up over the entire measurement time, as explained in Sect. 3.2.

The measurements of ice BTs are performed with increasing ground/ice temperatures over time. As the dielectric constant of the ice is not changing considerably as a function of its temperature, the dielectric constant used in the model is selected as for a temperature of 0 °C,  $\epsilon_{\text{ice}} = 3.1884 - 0.0085 \times i$ . Modelled BTs are obtained for a range of asphalt ground temperatures and by selecting the best ice surface roughness ( $\sigma_{\text{ice}}$ ) to fit the measured BTs at the corresponding ice thickness. The ice surface roughness,  $\sigma_{\text{ice}}$ , was found to be 0.41 mm for a thickness of 3 mm (ice a),  $\sigma_{\text{ice}} = 0.32$  mm for 6 mm (ice b), and  $\sigma_{\text{ice}} = 0.275$  mm for 8 mm (ice c). It appears that the thinner the ice, the higher the ice roughness and vice versa. Indeed, thick ice is formed from a few mm of liquid water and therefore presents lower surface roughness, while the roughness of a thinner ice layer will approach the roughness of the dry surface.

The model [29, 30, 33] fits the radiometric measurements with high accuracy for the various studied road conditions. Such a model is extremely useful to understand the physics of layered structures with rough boundaries and it permits the quantitative extraction of key parameters, as shown in Table 1.

### 4.3 Road Condition Emissivity

The emissivity ( $E_{\text{H,V}}$ ) depends on the reflection coefficient ( $R_{\text{H,Vrough}}$ ) as  $E_{\text{H,V}} = (1 - R_{\text{H,Vrough}})$ . Using Eq. (1), the emissivity can be written in terms of

**Table 1** Fitting parameters

Road condition	Angle $i$ (°)	Ground temp. (K)	Top layer roughness (mm)	Ground roughness (mm)	Top layer dielectric const
Dry a	56	222–295	-	0.668	8.9–0.72i
Dry b	50	225–295	-	0.668	8.9–0.72i
Water (liq.)	50	292.15	0–0.668	0.668	7.992–13.29i
Ice a	56	245–268	0.410	0.668	3.1884–0.0085i
Ice b	56	248–268	0.320	0.668	3.1884–0.0085i
Ice c	56	250–268	0.275	0.668	3.1884–0.0085i

the measured brightness temperatures as shown in Eq. (6). The ground temperatures used to calculate the emissivity were taken as the modelled temperatures from Table 1 for each road condition.

$$E_{H,V} = \frac{BT_{H,V} - T_{\text{sky}}}{T_{\text{ground}} - T_{\text{sky}}} \quad (6)$$

Measurements from Figs. 8 and 9 are presented in terms of emissivity in Fig. 10 together with their fitting curves. H-pol and V-pol emissivity's are easily distinguishable for the studied dry, liquid water, and ice road conditions. This way of presenting the surface properties is convenient as it depends on the characteristics of the surfaces and not on their physical temperature. However, it requires additional temperature sensor to measure the ground surface temperature.

## 5 Conclusions

This paper has studied the use of a 93-GHz passive dual-polarised radiometer to detect the presence of ice or liquid water on asphalt road surfaces. The brightness temperatures of dry, liquid water, and icy asphalt have been studied in laboratory conditions at two angles of observation.

The results showed that the studied surfaces are distinguishable both in terms of the measured H-pol and V-pol brightness temperatures or their emissivity. Indeed, dry asphalt has a higher H-pol brightness temperature than measured for ice and water. In the case of ice, the thickness of the ice sheet above the asphalt impacts the

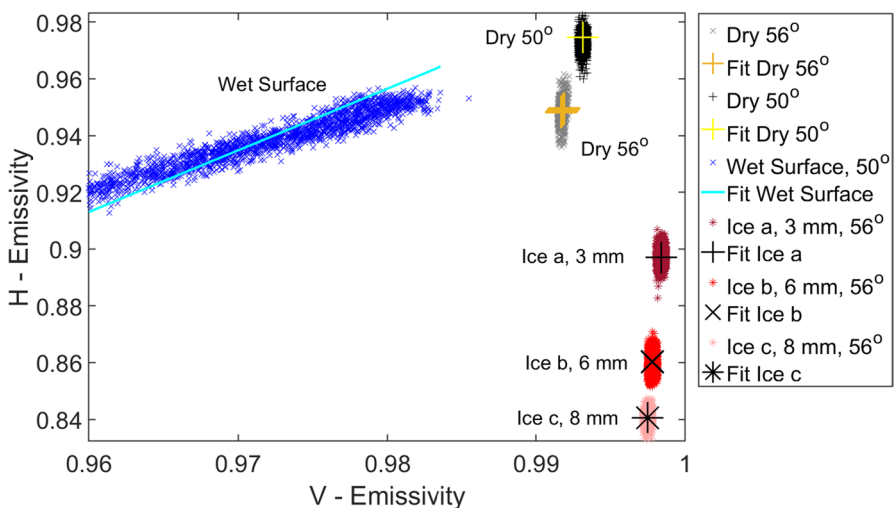


**Fig. 10** Measured  $H$ - $V$  emissivity fitted with modelled brightness temperatures from dry asphalt at 56° and 50° (grey & black—measured; orange & yellow—modelled), wet surface at 50° (blue—measured; cyan—modelled), and ice at 56° with thicknesses of 3, 6, and 8 mm (red—measured; black—modelled)



H-pol brightness temperature. The thicker ice layer has the lower H-pol brightness temperature as the air-ice boundary is smoother than for thinner ices. It was shown that a change of thickness of the liquid water on asphalt has a steep slope, going from a low H-pol and V-pol values (193 and 244 K, respectively) to the dry value at the same angle.

A coherent scattering model was used to describe the physics underlying the laboratory experiments. The modelled brightness temperatures fitted with the radiometric measurements provide qualitative values, such as surface roughness, surface temperatures, or dielectric constants. For example, the change of ice's thickness implies a change in the air-ice surface roughness, from 0.41 mm with 3-mm ice to 0.275 mm for an ice of 8 mm. For the liquid water, the decrease of its layer thickness corresponds to a change of the apparent surface roughness of the air–water boundary, from 0 mm to that of asphalt (0.668 mm).

Finally, the measurements of the H-pol and V-pol brightness temperatures were linked to the emissivity of the surfaces. The various conditions have distinct and well separated regions of emissivity, which makes possible to characterise road conditions based on measurements of surface emissivity. However, limitations could occur when the angle of observation of the instrument changes or if the road surface roughness is changing. The installation of the radiometer on a moving vehicle for real condition testing is required to confirm the potential of commercialisation of this technology for the automotive industry.

Another advantage of this experimental setup is its efficiency to determine the surface roughness of the dry road section. The radiometric results combined with the coherent scattering model gave a roughness value identical to the one measured with a 3-D scan of the surface. Using a radiometer is a non-destructive way of measuring the roughness and would enable to evaluate of when and where road surfaces would need to be replaced with a quick and simple measurement.

**Acknowledgements** We thank Sebastian Almfeldt, research engineer at Structural Engineering (Chalmers University of Technology), for his 3D measurement of the asphalt surface.

**Funding** Open access funding provided by Chalmers University of Technology. This work is supported by Swedish Strategic Vehicle Research and Innovation FFI grant 2018–02707.

**Data Availability** The datasets generated during and/or analysed during the current study are available from the corresponding author on reasonable request.

**Open Access** This article is licensed under a Creative Commons Attribution 4.0 International License, which permits use, sharing, adaptation, distribution and reproduction in any medium or format, as long as you give appropriate credit to the original author(s) and the source, provide a link to the Creative Commons licence, and indicate if changes were made. The images or other third party material in this article are included in the article's Creative Commons licence, unless indicated otherwise in a credit line to the material. If material is not included in the article's Creative Commons licence and your intended use is not permitted by statutory regulation or exceeds the permitted use, you will need to obtain permission directly from the copyright holder. To view a copy of this licence, visit <http://creativecommons.org/licenses/by/4.0/>.

## References

1. Global status report on road safety 2018: summary. Geneva: World Health Organization; 2018 (WHO/NMH/NVI/18.20). Licence: CC BY-NC-SA 3.0 IGO).
2. USDOT FHWA: <https://ops.fhwa.dot.gov>
3. A. Troiano, E. Pasero and L. Mesin, "An innovative water and ice detection system for monitoring road and runway surfaces," 6th Conference on Ph.D. Research in Microelectronics & Electronics, Berlin, 2010, pp. 1–4.
4. Tabatabai, H.; Aljuboori, M. A Novel Concrete-Based Sensor for Detection of Ice and Water on Roads and Bridges. *Sensors* **2017**, 17, 2912.
5. AURORA Group's "Standardized Testing Methodologies for Pavement Sensors" dated December 7, 1999
6. Kwon Tae Jung, Fu Liping, and Jiang Chaozhe. Road weather information system stations — where and how many to install: a cost benefit analysis approach. *Canadian Journal of Civil Engineering*. 42(1): 57–66. <https://doi.org/10.1139/cjce-2013-0569>
7. Innovative Dynamics, Inc., "Infrared Sensor for Pavement Ice Detection", IDI Technical Report, Ithaca New York, December 2001
8. Sakk, Eric, et. al, "Remote Sensors for Pavement Ice Detection Phase II SBIR Option", Final Report, Innovative Dynamics, Ithaca New York, October 2001.
9. Rios-Gutierrez, F.; Hassan, M.A. Survey and Evaluation of Ice/Snow Detection Technologies. Northland Advanced Transportation Systems Research Laboratories
10. G. Pan, L. Fu, R. Yu, M Muresan, "Winter Road Surface Condition Recognition Using a Pre-trained Deep Convolutional Neural Network", Transportation Research Board 97th Annual Meeting, 2018.
11. Y. Lu, et. al. "Black Ice Detection and Warning System", Patent application publication US2008/01129541 A1
12. K. Ueda, Y. Miyata, Y. Kandori, T. Tanizaki and T. Kamakura, "Discrimination Method of Water and Ice on Road Surfaces Using Quasi-millimeter Waves," Transactions of the Society of InstruV. Viikari, T. Varpula and M. Kantanen and Control Engineers, vol. 54, no. 3, pp. 331-339, Jan. 2018, <https://doi.org/10.9746/sicetr.54.331>.
13. H. Rudolf, G. Wanielik, A. J. Sieber, "Road condition recognition using microwaves." Proceedings of Conference on Intelligent Transportation Systems (1997): 996–999.
14. B. I. Tapkan, S. Yoakum-Stover, and R. F. Kubichek. "Active microwave remote sensing of road surface conditions," Proceedings, Snow Removal and Ice Control Technology, Fourth International Symposium (Reno, Nevada; August 11–16, 1996). Pages 73–80
15. N. Kees, J. Detlefsen, "Road Surface Classification by Using a Polarimetric Coherent Radar Module at MM-Wavelengths", IEEE M-S International Microwave Symposium Digest, 1994.
16. V. V. Viikari, T. Varpula and M. Kantanen, "Road-Condition Recognition Using 24-GHz Automotive Radar," in IEEE Transactions on Intelligent Transportation Systems, vol. 10, no. 4, pp. 639-648, Dec. 2009.
17. V. Vassilev, "Road Surface Recognition at mm-Wavelengths Using a Polarimetric Radar," in IEEE Transactions on Intelligent Transportation Systems, <https://doi.org/10.1109/TITS.2021.3066312>
18. J. Morland, J. Metcalfe and A. Walker, "Microwave remote sensing of soil moisture in southern Ontario: Aircraft and satellite measurements at 19 and 37 GHz," Radio Science, vol. 38, no. 4, pp. 8073, <https://doi.org/10.1029/2002RS002677>
19. S. Sandven, O.M. Johannessen and K. Kloster, "Sea Ice Monitoring by Remote Sensing", Encyclopedia of Analytical Chemistry, Sep. 2006, <https://doi.org/10.1002/9780470027318.a2320>
20. V.V. Sterlyadkin, "Radiometric microwave field measurements of the complex dielectric constant of the water surface", Advances in Space Research, Volume 62, Issue 11, 2018, Pages 3162–3169, ISSN 0273–1177, <https://doi.org/10.1016/j.asr.2018.08.040>.
21. O. Auriacombe, S. Rea, K. Parow-Souchon, M. Oldfield, A. Obeed, B. Davis, D. Cuadrado-Calle, M. Henry, H. Wang, N. Brewster, P. Hunyor, M. Merritt, D. Klugmann, M. Phillips, M. Beardsley, J. Hampton, B. Moyna, B. Ellison, C. Howe, G. Burton, A. Marshall, E. Johnson, B. Thomas, M. Brandt, M. Philipp, G. Sonnabend, T. Stangier, R. Hammett, G. Gissot, V. Kangas, S. D'Addio, P. Piironen, "Engineering Qualification Model (EQM) Front-End Receivers for the Microwave Imager and Microwave Sounder Instruments onboard MetOp-SG satellites," 2019 44th International Conference on Infrared, Millimeter, and Terahertz Waves (IRMMW-THz), 2019, pp. 1–1, <https://doi.org/10.1109/IRMMW-THz.2019.8874433>.

22. D. Cuadrado-Calle, S. Rea, O. Auriacombe, M. Oldfield, K. Parow-Souchon, A. Obeed, D. Klugmann, B. Rackauskas, B. Davis, P. Hunyor, M. Merritt, M. Phillips, M. Beardsley, W. Robins, J. Hampton, N. Brewster, P. Norbury, A. Cullum, H. Wang, M. Henry, A. Shepperd, D. Gerber, C. Howe, G. Burton, A. Marshall, T. Almond, D. Alves, E. Johnson, F. Aparicio, B. Moyna, B. N. Ellison, B. Thomas, M. Brandt, M. Philipp, G. Sonnabend, T. Stangier, A. Kilian, M. Trasatti, R. Hammett, P. Campbell, V. Kangas, P. Piironen, "EQM front-end receivers at 183 and 229 GHz for the Microwave Sounder on MetOp-SG," 2020 XXXIIIrd General Assembly and Scientific Symposium of the International Union of Radio Science, 2020, pp. 1-4, <https://doi.org/10.23919/URSIGASS49373.2020.9232214>.
23. Dr. P. Forkman, Onsala Space Observatory([peter.forkman@chalmers.se](mailto:peter.forkman@chalmers.se))
24. G. Macelloni, R. Ruisi, P. Pampaloni and S. Paloscia, "Microwave radiometry for detecting road ice," IEEE 1999 International Geoscience and Remote Sensing Symposium. IGARSS'99 (Cat. No.99CH36293), vol.2, pp. 891–893, Jul. 1999.
25. Y. Sasada, M. Nakano, Y. Miyata, K. Sugiyama and E. Shiba, "Development of the road surface condition sensing system," Proceedings 199 IEEE/IEEJ/JSAI International Conference on Intelligent Transportation Systems (Cat. No.99TH8383), pp. 14–19, Oct. 1999.
26. O. Auriacombe, V. Vassilev, A. Uz Zaman, "Oil, water, and ice detection on road surfaces with a millimeter-wave radiometer," Proc. SPIE 11533, Image and Signal Processing for Remote Sensing XXVI, 1153318 (20 September 2020)
27. F. T. Ulaby and D. G. Long, "Electromagnetic Wave Propagation," in Microwave radar and radiometric remote sensing, 4th ed., The University of Michigan Press, 2015.
28. A. Sihvola, "Mixing Rules with Complex Dielectric Coefficients." Subsurface Sensing Technologies and Applications **1**, 393–415 (2000).
29. F. Jonard, F. André, N. Pinel, C. Warren, H. Vereecken and S. Lambot, "Modeling of Multilayered Media Green's Functions With Rough Interfaces," in IEEE Transactions on Geoscience and Remote Sensing, vol. 57, no. 10, pp. 7671–7681, Oct. 2019, <https://doi.org/10.1109/TGRS.2019.2915676>.
30. A. Tabatabaenejad, X. Duan and M. Moghaddam, "Coherent Scattering of Electromagnetic Waves From Two-Layer Rough Surfaces Within the Kirchhoff Regime," in IEEE Transactions on Geoscience and Remote Sensing, vol. 51, no. 7, pp. 3943–3953, July 2013, <https://doi.org/10.1109/TGRS.2012.2229391>.
31. A. Voronovich, "Wave Scattering from Rough Surfaces", 2<sup>nd</sup> ed. (Springer, 1999).
32. N. Pinel, C. Bourlier and J. Saillard, "Degree of roughness of rough layers: Extensions of the rayleigh roughness criterion and some applications." Progress In Electromagnetics Research B., Jan. 2010, vol 19, pp. 41–63, <https://doi.org/10.2528/PIERB09110907>.
33. N. Pinel. "Extension of the scalar Kirchhoff approximation for calculating the coherent scattering from multi-layers with random rough interfaces." in International Geoscience and Remote Sensing Symposium (IGARSS), IEEE, Jul 2021, Brussels, Belgium. paper #1718
34. E. J. Jaselskis, J. Grigas and A. Brilingas, "Dielectric Properties of Asphalt Pavement", in Journal of Materials in Civil Engineering, Vol. 15 No. 5, p.p. 427–434, 2003

**Publisher's Note** Springer Nature remains neutral with regard to jurisdictional claims in published maps and institutional affiliations.